nature communications

Article

https://doi.org/10.1038/s41467-025-60823-0

Layered-columnar cathode materials for sodium-ion batteries

Received: 25 May 2024

Accepted: 3 June 2025

Published online: 01 July 2025

Check for updates

Xiaolin Zhao[1,2], Yi Li[1,2], Youwei Wang[1,2], Erhong Song[1,2], Ruguang Ma[3] ✉ & Jianjun Liu[1,2,4] ✉

The advancement of cathode materials possessing high-rate capability and extended cycle life is crucial for the viability of large-scale energy storage in sodium-ion batteries. A layered-columnar material $NaFe[O_3PCH(OH)CO_2]$ is designed with 2D grid-like channels for sodium ion migration. Operating on the Fe^{2+}/Fe^{3+} redox reaction, $NaFe[O_3PCH(OH)CO_2]$ exhibits a reversible specific capacity of 106.1 mAh g^{-1} after 50 cycles within the voltage range of 1.5–4.2 V, reaching 93.4% of the theoretical specific capacity. Experimental and theoretical investigations show that $NaFe[O_3PCH(OH)CO_2]$ exhibits low-strain characteristics during discharge and charge processes. The presence of stable C-P covalent bonds between organic layers and inorganic columns ($[FeO_6]$ and $[CPO_3]$) plays a pivotal role in achieving its long cycle life. Even under high current density of 240 mA g^{-1}, it maintains satisfactory capacities, delivering 61.6 mAh g^{-1} after the 1000th cycles, indicating a capacity retention rate of 92.2% with only 0.0078% loss per cycle. This study indicates that layered-columnar structure design offers a viable strategy for the development of high-performance positive electrode material for sodium-ion batteries.

Rechargeable sodium-ion batteries (SIBs) have garnered significant attention as a promising option for large-scale electrochemical energy storage due to the abundance and lower cost of sodium compared to lithium[1–3]. Several materials, including transition metal oxides[4,5], organic compounds[6,7], polyanionic compounds[8,9], and Prussian blue analogs[10] have been investigated as Na-ion host positive electrodes. Despite great advancements, cathode materials still encounter challenges such as limited insertion/extraction of Na-ions, irreversible phase transitions, and even structural collapse[11,12]. These issues could result in low capacity, serious battery polarization, and rapid capacity fading during cycling. Hence, there is a critical need for the development of advanced positive electrode materials, particularly those based on open structures.

The migration dynamics of sodium ions and stability of the structural framework play an important role in the energy density, long cycle life and high-rate performance of positive electrode materials. The Layered structures[13] with two-dimensional migration channels provide rapid ion transport, but they suffer from structural change even collapse during Na^+ de/intercalation. The tunnel structures[14] and olivine-type structures[15,16], characterized by one-dimensional diffusion channels, offer impressive cycle stability but at the cost of inherently slower ionic diffusion rates. Encouragingly, a layered-columnar structure containing organic phosphoric acids and metals can balance ionic migration with structural stability, which organic chains arranged in a layered periodic arrangement as the bottom and top of the layered-columnar structure, robust pillars composed of inorganic units that create 2D grid-like channels. The utilization of 2D grid-like channels facilitates rapid migration of Na^+ ions without destroying channel structure due to the flexibility of the organic chains and rigidity of pillars, thereby reducing strain and preventing collapse during cycling.

[1]State Key Laboratory of High Performance Ceramics and Superfine Microstructure, Shanghai Institute of Ceramics, Chinese Academy of Sciences, 1295 Dingxi Road, Shanghai 200050, China. [2]Center of Materials Science and Optoelectronics Engineering, University of Chinese Academy of Sciences, Beijing 100049, China. [3]School of Materials Science and Engineering, Suzhou University of Science and Technology, 99 Xuefu Road, Suzhou 215011, China. [4]School of Chemistry and Materials Science, Hangzhou Institute for Advanced Study, University of Chinese Academy of Sciences, 1 Sub-lane Xiangshan, Hangzhou 310024, China. ✉e-mail: ruguangma@usts.edu.cn; jliu@mail.sic.ac.cn

Herein, we present a positive electrode material with phosphoryl-based layered-columnar structure, $NaFe[O_3PCH(OH)CO_2]$, which demonstrates high specific capacity and long cycle life for sodium ion batteries. Through a one-step hydrothermal method, we synthesized a material with a stable framework and low strain that allows for reversible full charge and discharge of sodium ions. Based on the redox reaction of Fe^{2+}/Fe^{3+}, $NaFe[O_3PCH(OH)CO_2]$ exhibits a reversible specific capacity of 106.1 mAh g^{-1} after 50 cycles. The completely desodiumated structure, $Fe[O_3PCH(OH)CO_2]$, maintains kinetic stability and achieves long cycle life. Even at current density of 240 mA g^{-1}, the material displays satisfactory capacity retention of 92.2% with a specific capacity of 61.6 mA h g^{-1} after 1000th cycles, equivalent to a decay rate of 0.0078% per cycle. The Fe^{2+}/Fe^{3+} redox reaction, confirmed by both experimental XPS and calculated magnetic moments, is responsible for the high electrochemical performance of $NaFe[O_3PCH(OH)CO_2]$ in the voltage range of 1.5-4.2 V. DFT calculations show that the other layered-columnar structures $NaTM[O_3PCH(OH)CO_2]$ (TM= Mn, Co, Ni) have similar theoretical specific capacities and sodium ion migration barriers as $NaFe[O_3PCH(OH)CO_2]$. Meanwhile, the layered-columnar structures composed of 3-phosphonopropionic acid has a lower sodium ion migration barrier. This work demonstrates that designing layered-columnar structure is an effective route for developing high-performance positive electrode materials of sodium ion batteries.

Results

Structural characterization

As shown in Fig. 1a, the foundation of layered-columnar structures lies in organic phosphoric acid, particularly its phosphate groups (-PO_3) extending outward along the organic chain[17,18], which serve as the rigid pillars of the structural framework. These phosphate groups are inherently rigid, contributing to the stability of the framework. Particularly, the C-P bond in organophosphates exhibits ultra-high thermal stability[19], further enhancing the structural robustness. Consequently, 2-hydroxyphosphonoacetic acid (HPAA = $H_2O_3PCH(OH)CO_2H$)[20] has garnered attention, where phosphoryl of HPAA extending outward along the organic chain are able to form a layered-columnar structure with iron metal atoms. Moreover, inexpensive HPAA can be used to

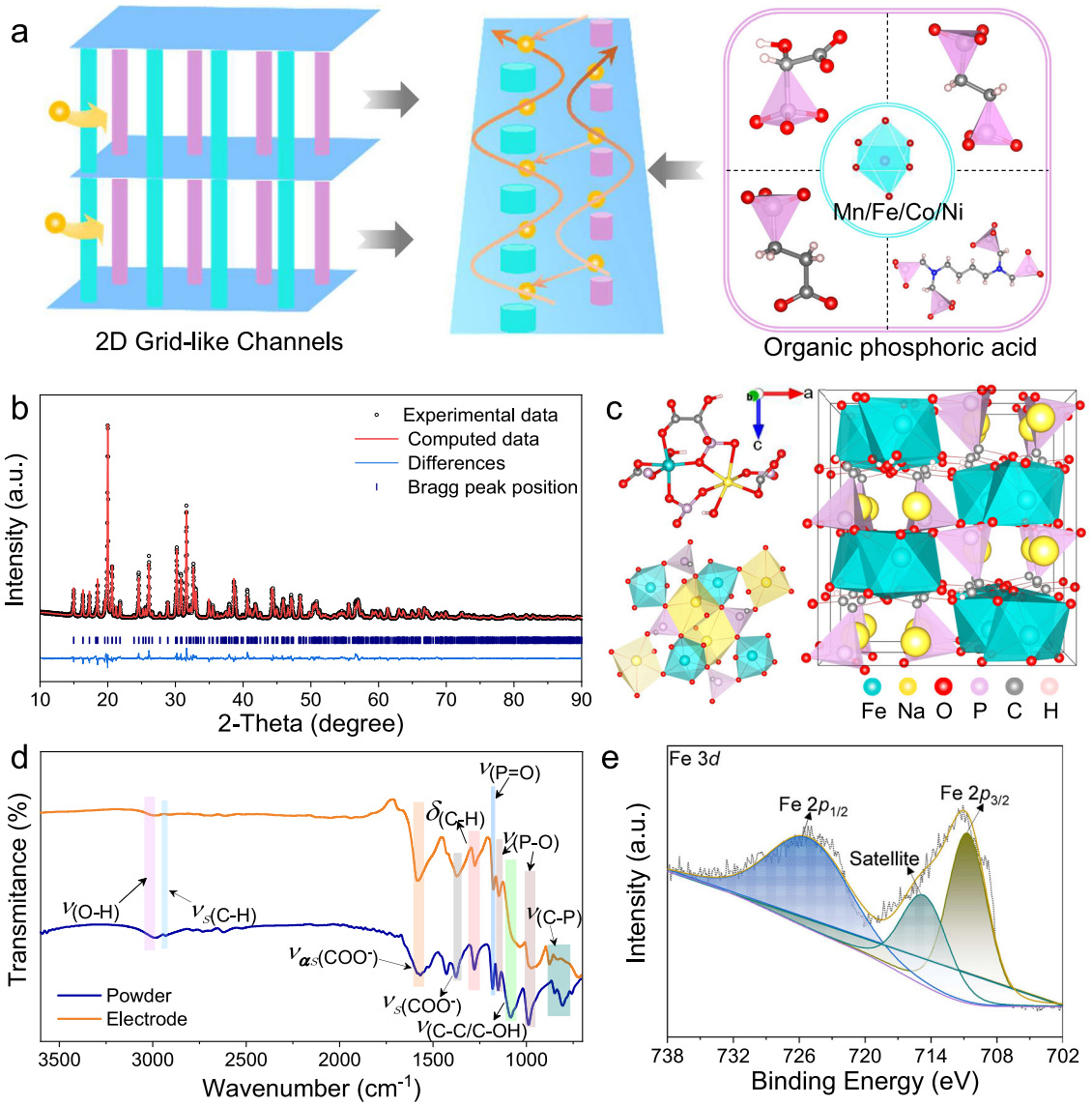

Fig. 1 | The structure analysis of $NaFe[O_3PCH(OH)CO_2]$. **a** The layered-columnar structure with 2D grid-like channels composed of metal and organic phosphoric acid. **b** Rietveld refinement of powder XRD Cu Kα. ($\lambda_{Cu\text{-}K\alpha}$ = 1.54056 Å) for $NaFe[O_3PCH(OH)CO_2]$ sample, experimental data in black dots, calculated curve in red and difference curve in olive. **c** The crystal structure of $NaFe[O_3PCH(OH)CO_2]$ along (010) direction. **d** Comparison of Fourier Transform Infrared Spectroscopy (FTIR) of $NaFe[O_3PCH(OH)CO_2]$ powder with $NaFe[O_3PCH(OH)CO_2]$ electrode. High-resolution X-ray Photoelectron Spectroscopy (XPS) of **e**. Fe 3 d.

form NaTM[$O_3PCH(OH)CO_2$] (TM= Mn, Fe, Co, Zn) materials with relatively high yields and favorable crystalline by the one-step hydrothermal method with transition metals[21]. The powder X-ray diffraction (PXRD) characterization of synthesized NaFe[$O_3PCH(OH)CO_2$] sample is performed and the powder XRD patterns are further analyzed by Rietveld refinement using FullProf software[22]. As shown in Fig. 1b and Table S1, the fitted curves are well consistent with the original XRD patterns with good reliability factor values (R_{wp} = 9.56%, R_p = 7.37%), demonstrating that the obtained single-phase samples are of high purity. As a result, the NaFe[$O_3PCH(OH)CO_2$] lattice is confirmed by Rietveld refinement to be an orthorhombic system of the *Pbca* space group with the lattice parameters a = 10.2608 Å, b = 9.7297 Å, c = 10.8549 Å and α = β = γ = 90°, consistent with previous X-ray diffraction results[23] (a = 10.267, b = 9.733 Å, c = 10.862 Å, α = β = γ = 90°). The three strongest diffraction peaks at 19.98°, 30.19°, and 31.62° correspond to the crystal planes (021), (222), and (213), respectively. The refined structure of NaFe[$O_3PCH(OH)CO_2$] formed by the phosphoryl organic and Fe^{2+} ions is shown in Fig. 1c, which contains polyanions and sodium cations. Organic chains (L = $O_3PCH(OH)CO_2$) are arranged in layers along the *c*-axis, with polyhedral [FeO_6] and [CPO_3] interlocking like pillars within the layers, forming a layered-columnar structure. Charging-compensated Na cations are located at the voids where the [CPO_3] tetrahedron are aligned along the *b*-axis. The [FeO_6] octahedra are distorted, a consequence of their coordination from three separate phosphonate ligands, two carboxylates and one hydroxyl. This coordination involves all the oxygen atoms from the L^{3-} ligand, which monodentately connect to iron ions. The Fe-O bond lengths in [FeO_6] range from 2.03 to 2.27 Å, which are close to the range of bond lengths in inorganic iron phosphate[24]. The [NaO_6] octahedron has four oxygens from phosphate and two from carboxylic acid and hydroxyl, respectively. Sodium ions are expected to migrate in the *ab* plane of the layered-columnar structure.

The chemical composition of the synthesized NaFe[$O_3PCH(OH)CO_2$] is investigated by FTIR analysis, as shown in Fig. 1d. There is only a medium band around 3003 cm^{-1}, which originates from the O-H stretching vibration of hydroxyl groups[25]. The peak at 2928 and 1273 cm^{-1} corresponds to C-H stretch vibration and bend vibration for alkyl groups[26]. Additionally, a very strong band around 1562 cm^{-1} and a medium band near 1370 cm^{-1} are attributed to the asymmetrical and symmetrical stretching vibrations of carboxylate group (-COO^-)[25,27,28]. There are also stretching vibration bands at 1176 cm^{-1} (υ(P=O))[21,28], 1144 cm^{-1} (υ(P-O))[21], 1076 cm^{-1} (υ(C-C/C-OH))[29,30], 980 cm^{-1} (υ(P-O))[21], 798 cm^{-1} (υ_s(C-P))[31]. In addition, NaFe[$O_3PCH(OH)CO_2$] electrode and pristine powder maintain the similar characteristic absorption peaks of the functional groups, including the vibrations peaks of O-H, C-H, -COO^- and -PO_3 group. These results indicate that the organic functional groups of HPAA are not destroyed during the electrode fabrication process. More importantly, the NaFe[$O_3PCH(OH)CO_2$] with layered-columnar framework structure is achieved by C-P and Fe-O-P bonds, exhibiting an obvious layered structure with alternating organic and inorganic arrangements, which benefits utilizing the advantages such as flexibility of organic structure, electrochemical activity and stability of inorganic structure. As shown in Fig. 1e and Fig. S1, five peaks corresponding to P, C, O, Fe, and Na of NaFe[$O_3PCH(OH)CO_2$] are observed. In addition, the peaks of Fe 2*p*3/2 and Fe 2*p*1/2 at 710.7 and 724.6 eV demonstrated the presence of Fe^{2+} in NaFe[$O_3PCH(OH)CO_2$][32,33]. TG-DSC and XRD curves of Fig. S2 showed that NaFe[$O_3PCH(OH)CO_2$] had almost no weight loss below 380 °C under N_2 atmosphere and the structural framework remains unchanged. It is not until 390 °C that NaFe[$O_3PCH(OH)CO_2$] an exothermic behavior with weight loss. High decomposition temperatures greater than 380 °C confirm the excellent chemical and thermal stability of NaFe[$O_3PCH(OH)CO_2$] with C-P and Fe-O-P bonds. The morphology of the synthesized NaFe[$O_3PCH(OH)CO_2$] is characterized by scanning electron microscopy (SEM) Figure S3. It exhibited a typically bulk morphology, composed of dense and thick sheets. Furthermore, STEM-EDX elemental mapping images and XRF (Table S2) verified the uniform distribution of C, O, P, Na, and Fe in NaFe[$O_3PCH(OH)CO_2$]. The homogeneous dispersion of Na and Fe elements reaffirms that the functional groups in organ-phosphines can effectively adsorb metal ions through strong coordination.

Electrochemical investigations

The electrochemical properties of NaFe[$O_3PCH(OH)CO_2$] positive electrodes are thoroughly studied in half-cells, within the working voltage range of 1.5–4.2 V (versus Na^+/Na). At a current density of 12 mA g^{-1}), the electrode delivered high capacities of 132.0, 107.9, and 106.1 mAh g^{-1} at the 1st, 2nd, and 50th cycle, respectively (Fig. 2a). The specific capacity of the conductive agent (Super P) during charging and discharging is only ~7 mAh g^{-1} in Figure S4, which means that it only plays a role in enhancing the conductivity of the active material. A irreversible capacity (24.1 mAh g^{-1}) is attributed to SEI film formation in the first cycle[34] and the irreversible specific capacity could be reduced by immersing the electrode into the electrolyte for a period of time before cycling. As shown in Figure S5, the infiltration of the electrolyte not only reduces the irreversible specific capacity of the NaFe[$O_3PCH(OH)CO_2$] (24.1 → 18.9 mAh g^{-1}), but also increases the discharge specific capacity of the NaFe[$O_3PCH(OH)CO_2$] (106.1 → 132.0 mAh g^{-1}) during the first 20 cycles. The specific capacity is very stable in the subsequent cycles, reaching 93.4% of the theoretical specific capacity (113.6 mAh g^{-1}), along with a high average Coulombic efficiency of 99.8%, indicating that the NaFe[$O_3PCH(OH)CO_2$] can achieve almost complete intercalation/de-intercalation of sodium ions. More importantly, NaFe[$O_3PCH(OH)CO_2$] has a higher reversible specific capacity than metal-organic framework materials $Na_2Fe(C_2O_4)F$ (69.4 mAh g^{-1})[35]、$Na_2Fe(C_2O_4)(HPO_4)$ (75 mAh g^{-1})[36] and $Na_2Fe(C_2O_4)(SO_4)\cdot H_2O$ (104 mAh g^{-1})[37]. Under electrochemical conditions, NaFe[$O_3PCH(OH)CO_2$] exhibits a reversible specific capacity of 137.5 mAh g^{-1} after 20 cycles as a positive electrode for Li-ion batteries, while also maintaining structural framework integrity (Fig. S6). Therefore, Li-ion battery positive electrode materials with layered-column structure can be prepared by electrochemical ion exchange method. The rate performance of NaFe[$O_3PCH(OH)CO_2$] positive electrode is plotted in Fig. 2b, c. The reversible discharge capacity of NaFe[$O_3PCH(OH)CO_2$] positive electrode is 89.1, 85.9, 83.5, and 81.8 mAh g^{-1} at current density of 24 mA g^{-1}, 36 mA g^{-1}, 48 mA g^{-1} and 60 mA g^{-1}, respectively. Meanwhile, the capacity gradually decreased as the current density continued increasing to 120 mA g^{-1}, 240 mA g^{-1}, and 360 mA g^{-1}, but also recovered to 94.0 mAh g^{-1} when the rate returned to 12 mA g^{-1}, indicating a favourable rate performance. Typical cyclic voltammogram (CV) curves of the NaFe[$O_3PCH(OH)CO_2$] electrode in 1st, 2nd, and 3rd cycles are recorded at a scan rate of 0.5 mV s^{-1} (Fig. 2d). During the de-intercalation/intercalation of Na-ions, a pair of peaks at 3.01/2.42 V is observed in the electrochemical processes, corresponding to Fe^{2+}/Fe^{3+} redox reaction. Based on the charge transfer resistance of the EIS at different temperature (Fig. S7 and Table S3), the activation energy (E_a) for sodium extraction/insertion is calculated. Obtained relatively high activation energy (~63.4 kJ mol^{-1}) for charge transfer may be the main reason for the voltage polarization[38]. The overlapping of these curves indicated the good cyclic stability of the positive electrode. In addition, the long-term cycling performance is investigated as well. In Fig. 2e, the initial increase in capacities is attributed to the activation process, where the Na-ion transport is gradually facilitated by increased contact between the active material and electrolyte. Under current density of 240 mA g^{-1}, NaFe[$O_3PCH(OH)CO_2$] achieved high capacities of 61.6 mAh g^{-1} and satisfactory capacity retention of 92.2% at the 1000th cycle. Therefore, layered-columnar structure enables high rate and high reversible specific capacity of polyanionic materials.

https://doi.org/10.1038/s41467-025-60823-0

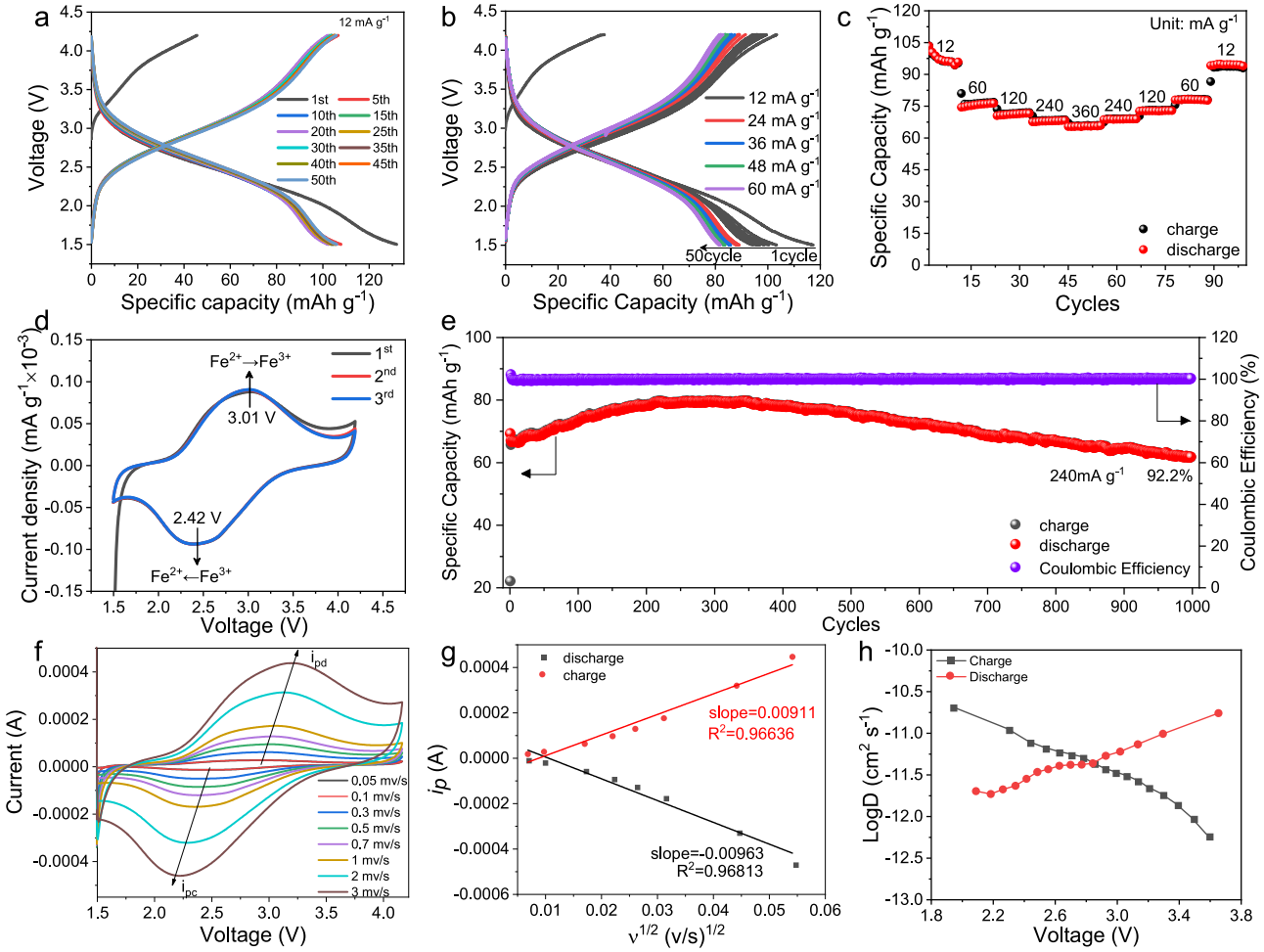

Fig. 2 | Electrochemical measurements of NaFe[O_3PCH(OH)CO_2] in Na half-cells. **a** Galvanostatic charge-discharge curves at 12 mA g^{-1}. **b** Galvanostatic charge-discharge curves for 50 cycles at different current densities of 12, 24, 36, 48 and 60 mA g^{-1}. **c** Rate performance under different current densities. **d** CV curves in different cycles at a scan rate of 0.5 mV s^{-1}. **e** Cycling performance at 240 mA g^{-1} for 1000 cycles. **f** CV curves of NaFe[O_3PCH(OH)CO_2] at scan rate of 0.05-3 mV s^{-1}, respectively. **g** The fitting curves between the peak current (I_P) and the square root of the scan rate ($v^{1/2}$). **h** Na^+ diffusion coefficient calculated from GITT curve as a function of voltage.

The CV curves at different scanning rates, Galvanostatic intermittent titration technique (GITT) and electrochemical impedance spectroscopy (EIS) are employed to study the migration dynamic of sodium ions in NaFe[O_3PCH(OH)CO_2]. The sodium ion diffusion coefficient D_{Na} can be calculated from the Randles-Sevcik equation:$I_P = 2.69 \times 10^5 n^{3/2} A C D_{Na}^{1/2} \nu^{1/2}$, I_P is the peak current (A), v is the potential scan rate (v s^{-1}), n is the total number of electrons reacted per mole in the electrochemical process ($n = 1$), A is the effective area of electrode (1.5386 cm^2), C is the intrinsic concentration of Na^+ (0.01255 mol cm^{-3}). Obtained the peak anodic and cathodic currents from the CV curves of NaFe[O_3PCH(OH)CO_2] at 0.05-3 mv s^{-1} (Fig. 2f), which are plotted as a linear function versus the square root of the scan rate in Fig. 2g. Substituting the slopes in Fig. 2g into Randles-Sevcik equation, the diffusion coefficient are 3.07×10^{-12} and 3.43×10^{-12} cm^2 s^{-1} for cathodic and anodic current peaks, respectively, which are in the same order of magnitude as the ion mobility coefficients obtained by ESI (2.24×10^{-12}) in Fig. S8. It is noteworthy that NaFe[O_3PCH(OH)CO_2] pellet without any additives and modifications have high intrinsic ionic conductivity (~10^{-5} S cm^{-1}) and low activation energy (0.195 eV) based on EIS tests (Fig. S9 and Table S4). As shown in Fig. 2h, the sodium ions diffusion coefficients between $10^{-12.2}$ and $10^{-10.6}$ cm^2 s^{-1} within the voltage window of 1.5–4.2 V are obtained based on the GITT curves of NaFe[O_3PCH(OH)CO_2] material for the charge and discharge at the 20 cycles (Fig. S10). More importantly, the migration coefficients of NaFe[O_3PCH(OH)CO_2] are of a similar order of magnitude to those of NASICON-type positive electrode materials as well as P2-phase layered materials (Table S5). Therefore, the excellent migration kinetics of NaFe[O_3PCH(OH)CO_2] is confirmed by EIS, CV curves and GITT analysis.

Characterization of structural evolution

In order to reveal the energy storage mechanism of NaFe[O_3PCH(OH)CO_2], in-situ XRD contour plots (Fig. 3a) are performed during the initial cycle and second charge processes to track the structural evolution of the material. As can be seen, the (200), (022), (212) and (241) peaks exhibited negligible shifts from pristine state to a charge of 4.2 V. Furthermore, there are no discernible changes during the Na^+ insertion processes even at low voltage of 1.5 V. In Fig. S11, the maximum variation values of lattice constants c, a and volume from charging (full detachment) to discharging (full insertion) obtained by Rietveld refinement method are 0.32%, −0.22%, and 0.11%, respectively. These findings demonstrate that the reversible extraction/insertion of Na ions does not cause a phase transition reaction in NaFe[O_3PCH(OH)CO_2], indicating that the material possesses excellent structural stability and rigidity. Further, FTIR analysis are conducted to examine the structural evolution of the NaFe[O_3PCH(OH)CO_2] electrode during the charging and discharge process (Fig. 3b). The analysis revealed a strong absorption band at 1576 cm^{-1} and medium

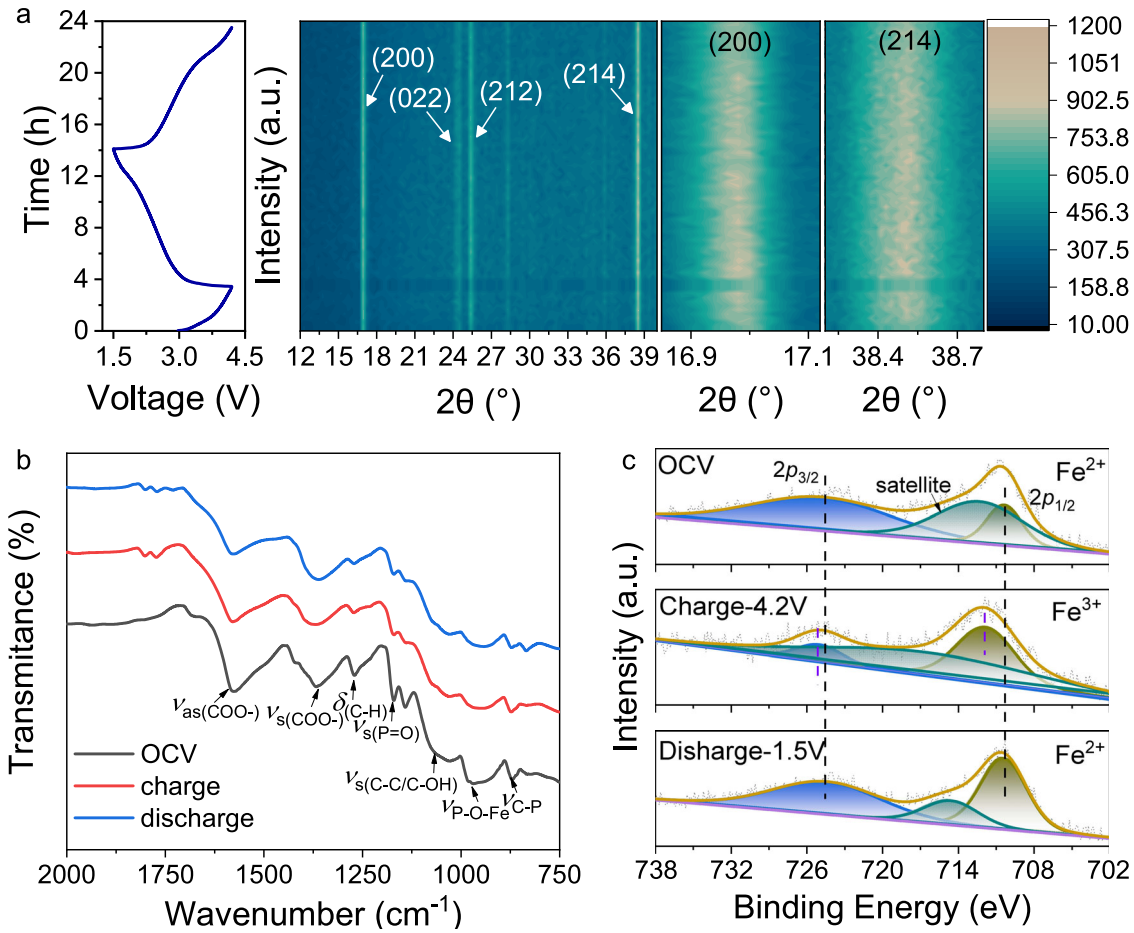

Fig. 3 | The structural evolution and redox mechanism of the NaFe[O_3PCH(OH)CO_2]. a *In*-situ XRD contour plots versus voltage profile of NaFe[O_3PCH(OH)CO_2] during the initial cycle and second charge. **b** Ex-situ FTIR spectrum of NaFe[O_3PCH(OH)CO_2] before and after charging and discharging. **c** The ex-situ high-resolution of Fe 2*p* during charging and discharging.

absorption bands near 1363 and 1268 cm^{-1}, which are attributed to the asymmetrical and symmetrical stretching vibrations of -COO^-, and the bending vibration of C-H. The P=O and P-O stretching and bending bands appeared in the region of 1195−980 cm^{-1} before discharge. It is noteworthy that new peaks at 1770 and 1799 cm^{-1} in the electrochemical process, which corresponding to the C=O stretching vibration mode of the EC molecule in electrolyte solutions[39,40]. The ex-situ XPS of C 1*s*, O 1*s* and Na 1*s* also confirmed the breakdown of the electrolyte. As shown in ex-situ XPS of Fig. S12, the C 1*s* spectra are mainly affected by the signals of the active material, binder (PVDF) and carbon additive constituents[41]. When charged to 4.2 V, a new peak appears at a binding energy of 290.4 eV in the O 1*s* spectra, which may correspond to the -C-O- functional group of alkoxy compounds[42]. Additionally, two characteristic peaks in the Na 1*s* spectra may be associated with $NaClO_4$/Na_2CO_3 and NaCl/NaF, suggesting the formation of CEI due to electrolyte decomposition. More importantly, the binding energies of ex-situ XPS still maintained the peaks corresponding to functional groups (-COO^-, C-H, C-P, P=O/P-O and Fe-O-P) that similar to the XPS of powder structures in Fig. S1, which indicate low activity of the organic ligands. When the NaFe[O_3PCH(OH)CO_2] electrode is charged to 4.2 V and discharged to 1.5 V, there are no changes in intensity of -COO^-, C-H, C-P and -PO_3^{2-} vibrational peaks of ex-situ FTIR, reflecting that organic building blocks (-COO^-, C-OH, C-P and -PO_3^{2-}) do not participate in electrochemical reactions at the voltage of 4.2–1.5 V.

The ex-situ high-resolution XPS results of Fe 2*p* in different charge/discharge status are analyzed and presented in Fig. 3c. The high-resolution Fe 2*p* spectrum from the pristine NaFe[O_3PCH(OH)CO_2] positive electrode displayed two peaks at 710.3 and 724.8 eV, corresponding to the $2p_{3/2}$ and $2p_{1/2}$ peaks for Fe^{2+}, respectively, along with a characteristic satellite peak at 712.3 eV. Upon charging to 4.2 V, the Fe $2p_{3/2}$ and Fe $2p_{1/2}$ binding energy shifted positively to 711.8 and 725.0 eV, indicating an increase in the Fe oxidation state from Fe^{2+} to Fe^{3+}. Furthermore, the valence state of Fe changed from +3 to +2 after discharging, consistent with the above CV shown in Fig. 2d. Therefore, the Fe cation is redox-active site. Based on the above analyses, the sodium storage mechanism of NaFe[O_3PCH(OH)CO_2] electrode upon the whole Na^+ extraction/insertion process could be described as followed: $NaFe^{2+}[O_3PCH(OH)CO_2] \leftrightarrow Na_{1-x}Fe_x^{3+}Fe_{1-x}^{2+}[O_3PCH(OH)CO_2] + xNa^+ + xe^-$.

Theoretical analysis of electrochemical activity

The periodic DFT calculations are performed to elucidate the electrochemical activity of NaFe[O_3PCH(OH)CO_2]. The unit cell parameters of NaFe[O_3PCH(OH)CO_2] are calculated as a = 10.087, b = 9.763 Å, c = 10.753 Å, α = β = γ = 90° and the maximum deviation from the experimental lattice parameter is 1.75%, indicating the accuracy of the DFT method. All possible configurations of Na_{1-x}Fe[O_3PCH(OH)CO_2] (x = 1/8, 2/8, ···, 7/8, 8/8) are then ranked according to the electrostatic energies obtained by Supercell software. In Fig. S13, there is only one most stable structure of Na_{1-x}Fe[O_3PCH(OH)CO_2] at x = 1/8, 2/8, 7/8 and 8/8. However, when x = 3/8, 4/8, 5/8 and 6/8, Na_{1-x}Fe[O_3PCH(OH)CO_2] has several structures and the top three structures with the lowest electrostatic energies at each concentration are used for DFT

https://doi.org/10.1038/s41467-025-60823-0

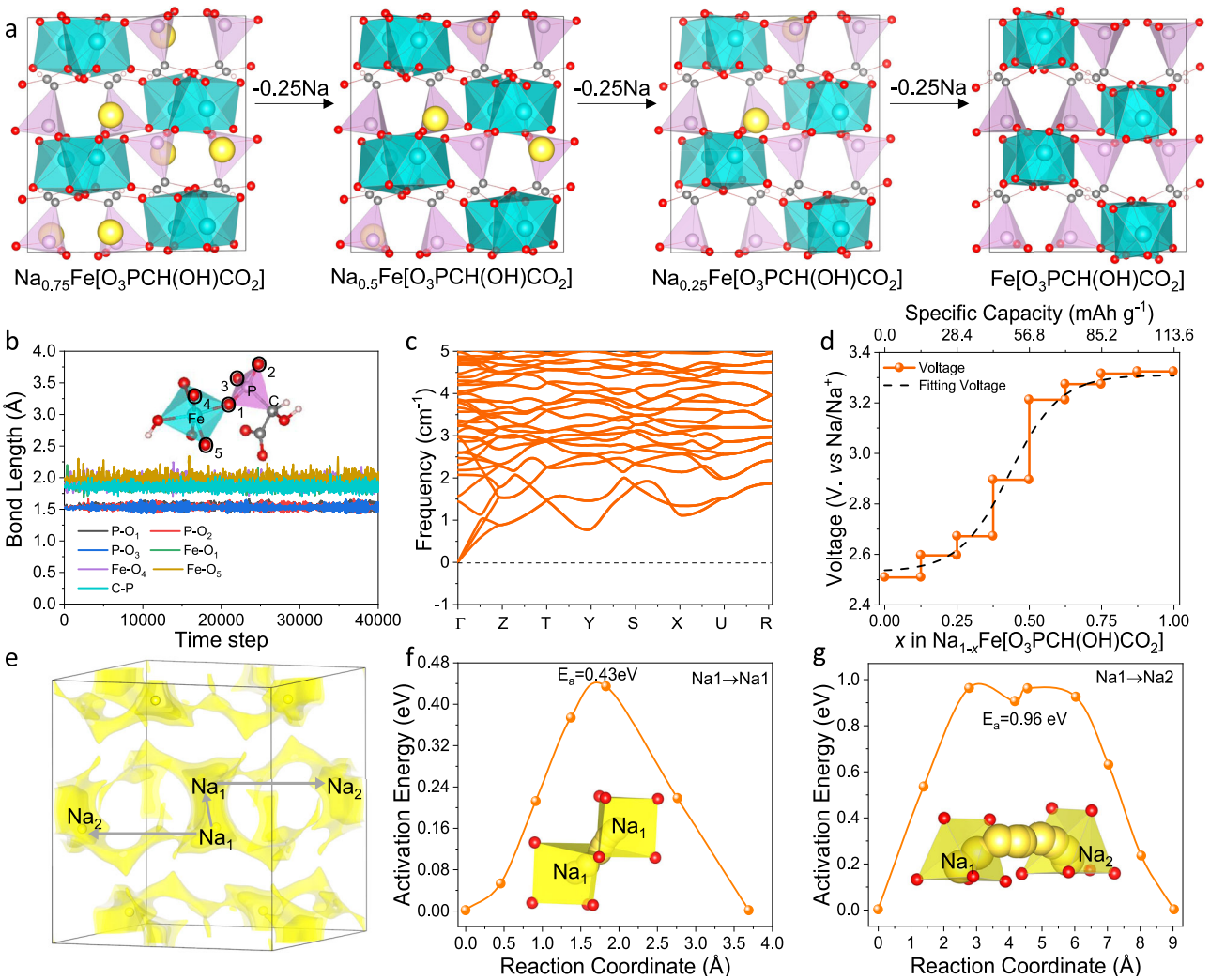

Fig. 4 | First principles calculation of $NaFe[O_3PCH(OH)CO_2]$. **a** The Na-ions de-intercalation sites and the structural evolution of $Na_{1-x}Fe[O_3PCH(OH)CO_2]$ (x = 2/8, 4/8, 6/8, 8/8). **b** The distributions of the Fe-O, C-P and P-O bond lengths in $Fe[O_3PCH(OH)CO_2]$ are calculated from AIMD simulations at 473 K. The inset shows the distribution of different chemical bonds in the structure. **c**. Phonon dispersions calculated by using the 2 × 2 × 2 supercell. **d** The calculated voltage plateaus of Na-ions extraction and the fitting voltage curve. **e** The 2D ionic conductivity pathways transport of sodium in $NaFe[O_3PCH(OH)CO_2]$ based on the BVSE calculations. BVEL maps with isosurfaces (yellow) drawn at the 0.05 eV level above E_{min}. Computed diffusion barrier of **f**. Na1 to Na1 **g**. Na1 to Na2. Na diffusion paths between the initial and final images are shown with yellow spheres in the unit cell.

calculations, corresponding the most stable structures of $Na_{1-x}Fe[O_3PCH(OH)CO_2]$ (x = 1/8, 2/8, ···, 7/8, 8/8) are shown in Fig. 4a and Fig. S14. Based on the de-intercalation sites of sodium ions, it is known that sodium ions are preferentially removed from the co-side configuration of $[NaO_6]$-$[NaO_6]$, which reduces the repulsive force between sodium ions. All sodium ions in the $Na_{1-x}Fe[O_3PCH(OH)CO_2]$ (x = 1/8, 2/8, ···, 7/8, 8/8) lattice are ordered to occupy the settled sites, so that all Na/vacancy are ordered in the ground state structure. As shown in Fig. S15, both the inorganic chain composed of $[FeO_6]$ and $[CPO_3]$ and the hydrogen bonding between the organic ligands along the b-direction can stabilize the desodiated structure. In addition, the average bond length of Fe-O in $[FeO_6]$ decreases during sodium ions removal (Fig. S16), which is attributed to the iron oxidation. The elongation of some P-O bonds (Fig. S17) in the local structure has the potential to compensate for the shortening of Fe-O bonds, resulting in little change in structural volume during sodium ion de-embedding. In Fig. 4b, the dynamic changes of the Fe-O, C-P, and P-O bond lengths in the completely sodium-free structure ($Fe[O_3PCH(OH)CO_2]$) at high temperature of 473 K reveal that rigid pillars vibrate only at equilibrium positions to maintain structural stability. The phonon spectra are analyzed to determine the kinetic stability of $Fe[O_3PCH(OH)CO_2]$. As shown in Fig. 4c, all phonon dispersion frequencies in the entire Brillouin zone are positive, indicating that the framework structure of $Fe[O_3PCH(OH)CO_2]$ is stable, which is the key factor for achieving full charge and discharge for long cycles in $NaFe[O_3PCH(OH)CO_2]$.

The voltages of $Na_{1-x}Fe[O_3PCH(OH)CO_2]$ (x = 1/8, 2/8, ···, 7/8, 8/8) based on the change of Gibbs free energy are further calculated using the formula $V = \frac{E_{Na_{1-x}Fe_2[O_3PCH(OH)CO_2]} + xE_{Na} - E_{Na_xFe_2[O_3PCH(OH)CO_2]}}{xe^-}$, with the reference to Na metal. The de-intercalation of sodium ions results in multiple voltage plateaus in the range of 2.51–3.32 V (Fig. 4d), which corresponds to the wide oxidation peak observed in the CV curve of Fig. 2d. The average charging voltage of 2.97 V is close to the experimental value of 3.01 V. It is worth mentioning that when sodium is used as a pseudo-reference electrode, its self-overpotential arises from kinetic limitations, surface side reactions and interfacial instabilities, resulting in deviations of its actual potential from the theoretical value. Despite the theoretical specific capacity of 113.6 mAh g^{-1} obtained from the de-intercalation of 8 Na-ions, the reversible specific capacity of 106.1 mAh g^{-1} achieved experimentally indicates almost full charge and discharge of the $NaFe[O_3PCH(OH)CO_2]$ layered-columnar material.

https://doi.org/10.1038/s41467-025-60823-0

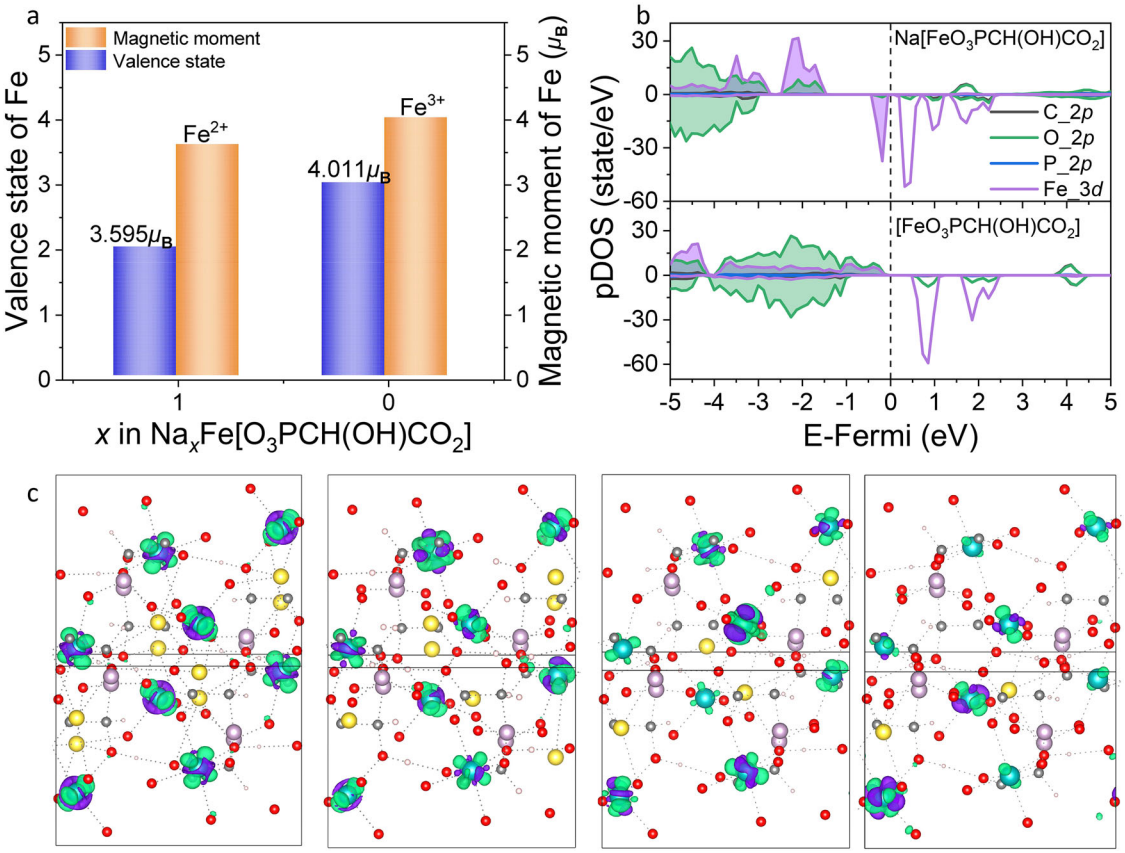

Fig. 5 | Evolution of the electronic structure in $NaFe[O_3PCH(OH)CO_2]$. a The changes in valence state and magnetic moment (μ_B) of Fe with the extraction of Na-ions. **b** Density of state of $Na_{1-x}Fe[O_3PCH(OH)CO_2]$ ($x = 0, 1$). Shaded areas indicate orbitals occupied by electrons and unshaded areas indicate orbitals not occupied by electrons. **c** The charge density difference of $Na_{1-x}Fe[O_3PCH(OH)CO_2]$ ($x = 0$, 0.25, 0.5, 0.75), green and purple represent the positive and negative 0.02 e/Å^3 isosurfaces, respectively. The yellow, red, cyan, gray, lavender and pink balls represent sodium, oxygen, iron, carbon, phosphorus and hydrogen atoms, respectively.

It is critical to elucidate the Na^+ diffusion mechanism in this newly designed $NaFe[O_3PCH(OH)CO_2]$ material. Therefore, the Na-ion mobility in the material is examined using a combination of the bond valence site energy (BVSE) method and the climbing image-nudged elastic band (CI-NEB) technique. Figure 4e shows the BVSE results on Na-ions mobility in the *ab* plane (yellow area). $NaFe[O_3PCH(OH)CO_2]$ has two distinguishable sodium sites, resulting in two kinds of Na^+ hopping pathways of Na1 → Na1 and Na1 → Na2. The CI-NEB of Fig. 4f, g displays the diffusion profiles of the octahedral-octahedral hopping paths (Na1 → Na1) and the neighboring octahedral sites (Na1 → Na2) of Na, respectively. The bottleneck size from Na1 → Na1 is larger than that of Na1 → Na2 (Fig. S18), resulting in a smaller migration energy barrier of Na1 → Na1 (0.43 eV) compared to that of Na1 → Na2 (0.96 eV) on the 2D grid-like channels. It is interesting to note that the migration barrier of sodium ions increases (0.43 → 0.89 eV) as the sodium ion content decreases (Fig. S19), which explains why the migration coefficient of sodium ions decreases during charging and increases during discharging (Fig. 2h). Thus, CINEB and BVSE calculations confirm that the layered-columnar structure favors the migration of sodium ions, resulting in a satisfactory sodium ion migration coefficient.

To elucidate the redox mechanisms underlying Na-ion extraction in $NaFe[O_3PCH(OH)CO_2]$, electronic structure analysis is carried out, including calculations of magnetic moment, density of states (DOS), and different charge density maps of $Na_{1-x}Fe[O_3PCH(OH)CO_2]$ ($x = 0$, 0.25, 0.5, 0.75), as depicted in Fig. 5. As shown in Fig. 5a, each iron atom in $NaFe[O_3PCH(OH)CO_2]$ and $Fe[O_3PCH(OH)CO_2]$ is in a high spin state with a magnetic moment of 3.595 μ_B and 4.011 μ_B, respectively, which are close to the magnetic moments of Fe^{2+} (3.6 μ_B) and Fe^{3+} (4.0 μ_B) in $[Fe_4^{2+}Fe_2^{3+}(OH)_{12}]^{2+}\cdot[CO_3^{2-}\cdot 3H_2O]$[43]. Therefore, the valence state of iron ions increases during the desodiumation process. It is worth mentioning that $NaFe[O_3PCH(OH)CO_2]$ and $Fe[O_3PCH(OH)CO_2]$ have the lowest energies when the spin states of the two neighboring irons are all antiparallel (Table S6), which is in accordance with the Goodenough-Kanamori-Anderson rule. In addition, Fe^{2+} is the redox active site of $NaFe[O_3PCH(OH)CO_2]$ during the processing of Na-ions extraction, which is also verified by DOS and different charge density map. The occupied orbitals of iron atoms are mainly distributed near the Fermi energy level (Fig. 5b), which is favorable for the loss of electrons during oxidation reactions. Following the extraction of sodium ions, the occupied orbitals of iron atoms become non-occupied. The differential charge density map in Fig. 5c clearly shows the charge transfer between iron and sodium atoms. The presence of sodium ions increases the positive charge of iron atoms in the $NaFe[O_3PCH(OH)CO_2]$ crystal structure, indicating that iron atoms gain electrons. As x increases from 0 to 0.75, the positive charge of some iron atoms in $Na_{1-x}Fe[O_3PCH(OH)CO_2]$ disappears, indicating the loss of electrons.

Mn, Co and Ni in the $NaTM[O_3PCH(OH)CO_2]$[21,44] family exhibit similar specific capacities as Fe, along with comparable two-dimensional migration barriers of sodium ions (Fig. S20). In addition, 3-phosphonopropionic acid can also be combined with transition metals such as Zn[45], V[46], and Cu[47] to create layered-columnar structures. As illustrated in Fig. S21a, the $[CPO_3]$ tetrahedra are alternately arranged with $[TMO_4]$ or $[TMO_6]$ units, while the charge-compensating sodium ions occupy the voids of the transition metal polyhedral layers.

The organic ligands serve as a binder linking the upper and lower polyhedral layers. BVSE calculations reveal that these layered-columnar structures feature two-dimensional sodium ion migration channels (Fig. S21b). The $NaVO[O_3P(CH_2)_2CO_2]$ structure exhibits the lowest two-dimensional migration barrier of 0.395 eV, as well as the shortest migration paths for $NaCu[O_3P(CH_2)_2CO_2]$. Consequently, the layered columnar structure not only enables the storage of ions based on the redox of active transition metals, but also the feature of low ion mobility barrier is expected to be applied in all-solid-state batteries.

Discussion

In this work, we synthesized the layered-columnar framework material $NaFe[O_3PCH(OH)CO_2]$ by one-step hydrothermal method to achieve high-rate capability and long cyclic life of phosphoryl Na^+-ion positive electrode material. The rigid inorganic chain composed of $[FeO_6]$ and $[CPO_3]$ and the hydrogen bonding between the organic ligands contributed to the kinetic stability of the fully desodiated structure $Fe[O_3PCH(OH)CO_2]$ after full charging. Electrochemical performance characterization revealed that $NaFe[O_3PCH(OH)CO_2]$ demonstrated a reversible specific capacity of 106.1 mAh g^{-1}, which is 93.4% of the theoretical specific capacity, after full charge and discharge of sodium ions. Additionally, the stable framework of the completely desodiated structure and the low strain of the structure during the charge and discharge allowed for long cycle life of $NaFe[O_3PCH(OH)CO_2]$, with satisfactory capacities of 61.6 mAh g^{-1} after the 1000th at current density of 240 mA g^{-1}, respectively. Furthermore, $NaFe[O_3PCH(OH)CO_2]$ exhibited a voltage plateau of 3.01 V generated by the redox of Fe^{2+}/Fe^{3+}, which meets the requirements of high voltage in positive electrode materials. In addition, DFT calculations reveal that the layered-columnar structures with the organic ligand of 3-phosphonopropionic acid have a lower sodium ion migration barrier, which are expected to be applied to all-solid-state batteries. Overall, this study demonstrates that designing phosphoryl layered-columnar materials provides an effective approach for developing high-performance positive electrode materials for sodium ion batteries.

Methods

Materials

$FeSO_4{\cdot}7H_2O$ (Aladdin, ≥99.95% metals basis), NH_4Cl (Aladdin, ≥99.99% metals basis), NaF (Aladdin, ≥99.99% metals basis) and $CH(OH)(CO_2H)(PO_3H_2)$ solution (Aladdin, 50% in H_2O) are purchased from Aladdin Shanghai. Deionized water from Milli-Q purification system. The purity of sodium metal negative electrode with a thickness of 0.45 ± 0.1 nm and a diameter of 15.6 mm is more than 99.7%, as supplied by Canrd.

Synthesis of $NaFe[O_3PCH(OH)CO_2]$

A mixture of $FeSO_4{\cdot}7H_2O$ (0.278 g, 1.0 mmol), NH_4Cl (4.86 g, 90 mmol), NaF (0.798 g, 19 mmol), $CH(OH)(CO_2H)(PO_3H_2)$ solution (1.4 mL, 2.0 mmol), and H_2O (20.0 mL) is stirred, then transferred to a 50 mL Teflon-lined stainless-steel autoclave and heated at 150 °C for 96 h. At the end of the hydrothermal reaction, a colorless precipitate and a yellowish supernatant are produced. The yellowish supernatant is an aqueous solution of unreacted 2-hydroxyphosphonoacetic acid, while the colorless precipitate is the target product $NaFe[O_3PCH(OH)CO_2]$. The colorless precipitate is extracted with a filter of SHB-III vacuum pump under constant rinsing with deionized water, further dried at 120 °C for 24 h to obtain pure colourless powders.

Electrochemical measurements

The active materials $NaFe[O_3PCH(OH)CO_2]$ are ball-milled with Super P (weight ratio of 7.5:2.5) at a speed of 400 rpm for 12 h in planetary ball mill (QM-3SP04). The obtained mixture is then mixed with Super P and polyvinylidene fluoride (PVDF, ARKEMA) binder that to dissolve in N-methyl-2-pyrrolidone (NMP: Aladdin, anhydrous ≥99.5%) solution at a weight ratio of 8:1:1, then evenly coated on the Al foil (16 μm thickness) by automatic coating machine (MSK-AFA-IIID) at 20 °C and dried in a vacuum oven at 100 °C for 12 h. The precision disc cutting machine (MSK-T10) is used to cut active material coated Al foil into uniformly sized positive electrode. The mass, diameter and thickness of the active materials in positive electrodes are 2.7 ± 0.3 mg, 14 mm and 20 μm. The sodium metal negative electrode covered with a removable protective film which protects the sodium metal from oxidation and can be removed before assembling the coin cells.

The CR2032 coin cells are assembled in an argon-filled glovebox where the content of O_2 and H_2O is less than 0.1 ppm. The cells are composed of Na negative electrode, $NaFe[O_3PCH(OH)CO_2]$ positive electrode, Waterman GF/C glass fiber separators (16 mm diameter) and 150 μl cm^{-2} electrolyte (1 mol/L $NaClO_4$ in a 1:1 mixture of ethylene carbonate (EC) and dimethyl carbonate (DMC) with 5.0% FEC). $NaFe[O_3PCH(OH)CO_2]$ positive electrode is also transferred to a coin-type cell (CR2032) using a Li metal negative electrode and 1 M LiPF6 in a 1:1 volumetric mixture of ethylene carbonate (EC) and ethyl methyl carbonate (EMC) electrolyte. Galvanostatic discharge-charge tests are performed at 25 ± 2 °C using LAND electrochemical testing system in battery thermostat box (LBI-300CH). Cyclic voltammetry (CV) measurements are carried out on Bio-logic VSP between 1.5 V and 4.2 V at a scan rate of 0.5 mV s^{-1}. We conduct multiple batches of electrochemical performance tests on the coin cells to ensure the reliability and reproducibility of the results.

The $NaFe[O_3PCH(OH)CO_2]$ powders are cold pressed into the sheet with a thickness of 0.062 cm and an area of 1.304 cm^2 under 270 MPa. Ionic conductivity of $NaFe[O_3PCH(OH)CO_2]$ sheet without any additivity and modification is determined using electrochemical impedance spectroscopy (EIS), which is conducted over a frequency range of 1 MHz to 10 Hz, with an amplitude of 10 mV and 10 points per decade at a quasi-stationary potential condition after open-circuit voltage for 5 minutes via an AUTOLAB PGSTAT302N electrochemical workstation. In addition, the EIS of a coin cell consisting of a $NaFe[O_3PCH(OH)CO_2]$ positive, a Na negative and electrolytes is also tested at a frequency range of 0.01–10^6 Hz, utilizing an amplitude of 10 mV and 10 points per decade. The coin cells are allowed to equilibrate at open-circuit voltage for 5 min before beginning the EIS measurements.

Characterizations

The crystal structures of materials are examined by powder X-ray diffraction (XRD, Bruker D8 Advance) using Cu Kα ($\lambda_{Cu\text{-}K\alpha}$ = 1.54056 Å) radiation between 10° and 90° with a scan speed of 2° min^{-1}. The Rietveld refinement for crystal structure is conducted by using FullProf program[22] with the Thompson–Cox–Hastings pseudo-Voigt peak shape functions[48]. For in-situ XRD experiments we have developed our own 35 mm inner diameter electrochemical cell, equipped with a Be window as a current collector, operating in reflection geometry. The in-situ cell is charged/discharged at current density of 12 mA g^{-1} with a sampling interval of 30 min for X-ray collection. The morphology of the samples is investigated by scanning electron microscope (SEM, FEI Verios G4). The elemental distribution is characterized by energy dispersive spectrograms (EDS). The samples used for both the ex-situ XPS and ex-situ FTIR spectroscopy measurements are obtained from positive electrodes in coin cells with different states of charge and discharge. Each coin cell after 5 h of resting is discharged/charged to the target voltage at current density of 12 mA g^{-1}. Subsequently, the cells are disassembled in a glove box filled with argon ($H_2O \le 0.1$ ppm, $O_2 \le 0.1$ ppm) to obtain positive electrodes. All positive electrodes are washed three times with 1,2 dimethylethane (DME) and subsequently dried in a vacuum at 60 °C for 12 h to eliminate any remaining solvents. These positive electrodes are exposed to air for less than 5 s. XPS measurements are conducted using an ESCALAB Xi+ X-ray photoelectron

spectrometer (Thermo Fischer, USA) employing Al K_α *X*-ray radiation ($h\nu$ = 1486.6 eV). Thermo Avantage software is used for data acquisition and subsequent processing. Fourier transform infrared spectroscopy (FTIR) measurements are performed using a Thermo Scientific Nicolet iS20 spectrometer equipped with a diamond ATR module. The wavelength range is 4000 to 750 cm^{-1} with a resolution of 4 cm^{-1} and 32 scans. Thermal analyses (TG-DSC) are carried out using a HITACHI STA200 simultaneous thermal analyzer. Samples (10 mg) are placed in a Al_2O_3 crucible with an identical and empty crucible used as the reference, and heated from 25 °C to 800 °C at a rate of 10 °C per minute in a nitrogen atmosphere.

Density functional theory calculations

The first-principles calculations are conducted within the formalism of spin-polarization density functional theory (DFT) and the generalized gradient approximation (GGA) of the exchange-correlation function as formulated by Perdew, Burke, and Ernzerhof[49]. The valence electron −ion interaction is treated by the projector augmented wave (PAW) potential[50] in the Vienna Ab initio Simulation Package (VASP)[51,52]. The van der Waals-augmented density functional theory (vdW-DFT) is used to modify exchange and correlation energies[53]. For the organic materials, the function of DFT is limited because of the proverbially poor ability to depict the long-range van der Waals (vdW) interaction between the molecules[54]. So the empirical dispersions of Grimme (DFT-D2) is applied to account for the long-range vdW interactions[55]. The DFT + U approach has been successfully applied in systems with strongly correlated *d* and *f* electrons. The U_{eff} values of 3.9 for Fe are taken.

The wave functions are expanded in plane-wave basis set up to a kinetic energy cutoff of 520 eV. Brillouin-zone integrations are performed by using the k-point sampling of the Monkhorst-Pack scheme with a 2 × 2 × 2 grid[56]. The convergence of total energy with respect to the kinetic energy cutoff and the k-point sampling has been carefully examined. The convergence criterion of energy and structural relaxation are set as less than 1.0×10^{-5} eV and 0.01 eV/Å, respectively. Minimization of the total energy is realized with a full relaxation of the atomic positions and cell parameters for each structure.

Ab initio molecular dynamics (AIMD) simulations are conducted for a duration of 20 ps at a temperature of 473 K, utilizing an NVT ensemble[57]. This NVT ensemble maintains constant values for the number of atoms (N), volume (V), and temperature (T) within the system. Bond lengths are measured at every time step, which is set to 0.5 fs. To control computational expenses, a G-centered k-point mesh of 1 × 1 × 1 is employed for sampling the Brillouin zone within a 1 × 1 × 1 crystal cell.

The phonon dispersion calculations are performed by using the Parlinski–Li–Kawazoe methodology implemented in the PHONOPY code[58], based on the Hellmann–Feynman forces calculated with the VASP code. The force constants are determined from the Hellmann–Feynman forces induced by the displacement of an atom in a sufficiently large supercell (2 × 2 × 2). The phonon frequencies and polarization vectors are then obtained by diagonalizing the dynamical matrices. In this work, the atomic displacements are set to 0.01 Å. The minimum energy path (MEP) for Na-ions migration is obtained from the climbing image nudged elastic band (CINEB)[59] method with a force convergence tolerance of 0.01 eV $Å^{-1}$. The BVSE calculations are performed using the SoftBV code[60] and the visualization of isosurfaces is carried out using VESTA software[61].

Data availability

The data generated from this study are included in the Supplementary Information/Source Data file. Source data for this study are also available as a separate Source Data file with this paper. Source data are provided with this paper.

References

1. Hwang, J. Y., Myung, S. T. & Sun, Y. K. Sodium-ion batteries: present and future. *Chem. Soc. Rev.* **46**, 3529–3614 (2017).
2. Vaalma, C., Buchholz, D., Weil, M. & Passerini, S. A cost and resource analysis of sodium-ion batteries. *Nat. Rev. Mater.* **3**, 18013 (2018).
3. Nayak, P. K., Yang, L., Brehm, W. & Adelhelm, P. From Lithium-Ion to Sodium-Ion Batteries: Advantages, Challenges, and Surprises. *Angew. Chem. Int Ed. Engl.* **57**, 102–120 (2018).
4. Su, H., Jaffer, S. & Yu, H. Transition metal oxides for sodium-ion batteries. *Energy Stor. Mater.* **5**, 116–131 (2016).
5. Gao, R.-M. et al. Recent advances and prospects of layered transition metal oxide cathodes for sodium-ion batteries. *Energy Stor. Mater.* **30**, 9–26 (2020).
6. Rajagopalan, R., Tang, Y., Jia, C., Ji, X. & Wang, H. Understanding the sodium storage mechanisms of organic electrodes in sodium ion batteries: issues and solutions. *Energy Environ. Sci.* **13**, 1568–1592 (2020).
7. Wang, H. G. & Zhang, X. B. Organic Carbonyl Compounds for Sodium-Ion Batteries: Recent Progress and Future Perspectives. *Chemistry* **24**, 18235–18245 (2018).
8. Zhang, H., Tan, X., Li, H., Passerini, S. & Huang, W. Assessment and progress of polyanionic cathodes in aqueous sodium batteries. *Energy Environ. Sci.* **14**, 5788–5800 (2021).
9. Barpanda, P., Lander, L., Nishimura, S. -i & Yamada, A. Polyanionic Insertion Materials for Sodium-Ion Batteries. *Adv. Energy Mater.* **8**, 1703055 (2018).
10. Peng, J. et al. Prussian Blue Analogues for Sodium-Ion Batteries: Past, Present, and Future. *Adv. Mater.* **34**, e2108384 (2022).
11. Xu, G. L. et al. Native lattice strain induced structural earthquake in sodium layered oxide cathodes. *Nat. Commun.* **13**, 436 (2022).
12. Jo, M. R. et al. Triggered reversible phase transformation between layered and spinel structure in manganese-based layered compounds. *Nat. Commun.* **10**, 3385 (2019).
13. Deng Y. P. et al. Layer-Based Heterostructured Cathodes for Lithium-Ion and Sodium-Ion Batteries. *Adv. Funct. Mater.* **29**, 1808522 (2019).
14. Liang X., Kim H., Jung H. G. & Sun Y. K. Lithium-Substituted Tunnel/Spinel Heterostructured Cathode Material for High-Performance Sodium-Ion Batteries. *Adv. Funct. Mater.* **31**, (2020).
15. Tripathi R., Wood S. M., Islam M. S. & Nazar L. F. Na-ion mobility in layered Na_2FePO_4F and olivine $Na[Fe,Mn]PO_4$. *Energy Environ. Sci.* **6**, 2257–2264 (2013).
16. Xiang, K. et al. Accommodating High Transformation Strains in Battery Electrodes via the Formation of Nanoscale Intermediate Phases: Operando Investigation of Olivine $NaFePO_4$. *Nano Lett.* **17**, 1696–1702 (2017).
17. Maeda, K. Metal phosphonate open-framework materials. *Microporous Mesoporous Mater.* **73**, 47–55 (2004).
18. Goura, J. & Chandrasekhar, V. Molecular metal phosphonates. *Chem. Rev.* **115**, 6854–6965 (2015).
19. Horsman, G. P. & Zechel, D. L. Phosphonate Biochemistry. *Chem. Rev.* **117**, 5704–5783 (2017).
20. Zhang, Q. Y., Mo, J. S. & Zhang, G. X. Study of Microwave Synthesis of 2 - Hydroxy Phosphono Acetic Acid Process. *Adv. Mater. Res.* **581-582**, 219–222 (2012).
21. Lai, Z., Fu, R., Hu, S. & Wu, X. Syntheses, Crystal Structures, Thermal Stabilities, and Magnetic and Luminescent Properties of 3D Heterometal Phosphonates: $NaM[O_3PCH(OH)CO_2]$ (M = Mn, Fe, Co, Zn). *Eur. J. Inorg. Chem.* **2007**, 5439–5446 (2007).
22. Rodríguez-Carvajal, J. Recent advances in magnetic structure determination by neutron powder diffraction. *Phys. B: Condens. Matter* **192**, 55–69 (1993).

23. Li, J., Zhu, Y.-Y., Huang, C.-Y., Sun, Z.-G. & Dong, D.-P. Poly[sodium [μ_4-2-hydroxyphosphonoacetato(3−)]iron(II)]. *Acta Crystallogr. Sect. E Struct. Rep. Online* **63**, m2350–m2350 (2007).
24. Xie, B. et al. Cathode Properties of $Na_3FePO_4CO_3$ Prepared by the Mechanical Ball Milling Method for Na-ion Batteries. *Sci. Rep.* **10**, 3278 (2020).
25. Colodrero, R. M. P. et al. Common Structural Features in Calcium Hydroxyphosphonoacetates. A High-Throughput Screening. *Cryst. Growth Des.* **11**, 1713–1722 (2011).
26. Yu Y. et al. Stabilizing Zn metal anode by interfacial self-assembled zincophilic metal-organic complex conversion layers. *Energy Stor. Mater.* **71**, 103601 (2024).
27. Colodrero, R. M. P. et al. Multifunctional Luminescent and Proton-Conducting Lanthanide Carboxyphosphonate Open-Framework Hybrids Exhibiting Crystalline-to-Amorphous-to-Crystalline Transformations. *Chem. Mater.* **24**, 3780–3792 (2012).
28. Demadis, K. D., Papadaki, M., Raptis, R. G. & Zhao, H. Corrugated, Sheet-Like Architectures in Layered Alkaline-Earth Metal R,S-Hydroxyphosphonoacetate Frameworks Applications for Anticorrosion Protection of Metal Surfaces. *Chem. Mater.* **20**, 4835–4846 (2008).
29. Wang, K. & Liu, Q. Chemical structure analyses of phosphorylated chitosan. *Carbohydr. Res* **386**, 48–56 (2014).
30. Wei Y. et al. Synthesis of a New Phosphonate-Based Sorbent and Characterization of Its Interactions with Lanthanum (III) and Terbium (III). *Polymers* **13**, 1513 (2021).
31. Somov, N. V. et al. Synthesis, structure, and properties of nitrilotris(methylenephosphonato)-triaquairon(II) {Fe[μ-NH(CH2PO3H)3](H2O)3}, as an ingredient of anticorrosive protective coatings on the steel surface. *Crystallogr Rep.* **60**, 853–859 (2015).
32. Jiang, Y. et al. Heterostructured Bimetallic MOF-on-MOF Architectures for Efficient Oxygen Evolution Reaction. *Adv. Mater.* **36**, e2306910 (2024).
33. Yang, C. et al. A semiconducting layered metal-organic framework magnet. *Nat. Commun.* **10**, 3260 (2019).
34. An, S. J. et al. The state of understanding of the lithium-ion-battery graphite solid electrolyte interphase (SEI) and its relationship to formation cycling. *Carbon* **105**, 52–76 (2016).
35. Yao, W. et al. $Na_2Fe(C_2O_4)F_2$: A New Iron-Based Polyoxyanion Cathode for Li/Na Ion Batteries. *Chem. Mater.* **29**, 2167–2172 (2017).
36. Pramanik, A., Bradford, A. J., Lee, S. L., Lightfoot, P. & Armstrong, A. R. $Na_2Fe(C_2O_4)(HPO_4)$: a promising new oxalate-phosphate based mixed polyanionic cathode for Li/Na ion batteries. *J. Phys.: Mater.* **4**, 024004 (2021).
37. Song, T. et al. A Low-Cost and Environmentally Friendly Mixed Polyanionic Cathode for Sodium-Ion Storage. *Angew. Chem. Int Ed. Engl.* **59**, 740–745 (2020).
38. Liao, L. et al. Effects of temperature on charge/discharge behaviors of LiFePO4 cathode for Li-ion batteries. *Electrochim. Acta* **60**, 269–273 (2012).
39. Ikezawa, Y. & Nishi, H. In situ FTIR study of the Cu electrode/ethylene carbonate+dimethyl carbonate solution interface. *Electrochim. Acta* **53**, 3663–3669 (2008).
40. Wang, L. et al. Identifying the components of the solid-electrolyte interphase in Li-ion batteries. *Nat. Chem.* **11**, 789–796 (2019).
41. Doubaji, S. et al. Passivation Layer and Cathodic Redox Reactions in Sodium-Ion Batteries Probed by HAXPES. *ChemSusChem* **9**, 97–108 (2015).
42. He, J., Tao, T., Yang, F. & Sun, Z. Optimizing the Electrolyte Systems for $Na_3(VO_{1-x}PO_4)_2F_{1+2x}$ ($0 \le x \le 1$) Cathode and Understanding their Interfacial Chemistries Towards High-Rate Sodium-Ion Batteries. *ChemSusChem* **15**, e202102522 (2022).
43. Polly, R. et al. First Principle Investigation of the Incorporation of Trivalent Lanthanides and Actinides in Hydroxycarbonate and Hydroxychloride Green Rust. *J. Phys. Chem. C.* **126**, 8016–8028 (2022).
44. Cui, L. et al. Hydrothermal syntheses, crystal structures, and thermal stability of two new 3D open-framework metal(II) phosphonates. *J. Coord. Chem.* **60**, 1247–1254 (2007).
45. Zhang, X. M. A Microporous Zinc Phosphonocarboxylate with a Zeolite ABW Framework via the Trialkyl Phosphonocarboxylate Route: In situ Synthesis and Characterization of $Na[Zn(O_3PC_2H_4CO_2)]\cdot H_2O$. *Eur. J. Inorg. Chem.* **2004**, 544–548 (2004).
46. Riou-Cavellec, M., Sanselme, M. & FeÂrey, G. Hybrid open frameworks: synthesis, structure and thermal behaviour of MIL-26, a new three-dimensional vanadium(IV) ethylcarboxyphosphonate $Na[V^{IV}O(O_3P(CH_2)_2CO_2)]2H_2O$. *J. Mater. Chem.* **10**, 745–748 (2000).
47. Riou-Cavellec, M., Sanselme, M. & Guillou, N. Fe´rey Gr. Hydrothermal Synthesis and ab Initio Structural Resolution from X-ray Powder Diffraction of a New Open Framework Cu(II) Carboxyethylphosphonate: $Na[Cu(O_3P\text{-}(CH_2)_2\text{-}CO_2)]$. *Inorg. Chem.* **40**, 723–725 (2001).
48. Thompson, P., Cox, D. E. & Hastings, J. B. Rietveld refinement of Debye–Scherrer synchrotron X-ray data from Al2O3. *J. Appl. Crystallogr.* **20**, 79–83 (1987).
49. Perdew, J. P., Burke, K. & Ernzerhof, M. Generalized gradient approximation made simple. *Phys. Rev. Lett.* **77**, 3865–3868 (1996).
50. Perdew, J. P. et al. Atoms, molecules, solids, and surfaces: Applications of the generalized gradient approximation for exchange and correlation. *Phys. Rev. B* **46**, 6671–6687 (1992).
51. Kresse, G. & Furthmuller, J. Efficiency of ab-initio total energy calculations for metals and semiconductors using a plane-wave basis set. *Comput. Mater. Sci.* **6**, 15–50 (1996).
52. Kresse, G. & Furthmuller, J. Efficient iterative schemes for ab initio total-energy calculations using a plane-wave basis set. *Phys. Rev. B* **54**, 11169–11186 (1996).
53. Savasta, S., Di Stefano, O., Savona, V. & Langbein, W. Quantum complementarity of microcavity polaritons. *Phys. Rev. Lett.* **94**, 246401 (2005).
54. Hobza, P., Sponer, J. & Reschel, T. Density-Functional Theory and Molecular Clusters. *J. Comput. Chem.* **16**, 1315–1325 (1995).
55. Grimme, S. Semiempirical GGA-type density functional constructed with a long-range dispersion correction. *J. Comput. Chem.* **27**, 1787–1799 (2006).
56. Monkhorst, H. J. & Pack, J. D. Special points for Brillouin-zone integrations. *Phys. Rev. B* **13**, 5188–5192 (1976).
57. Martyna, G. J., Klein, M. L. & Tuckerman, M. Nosé–Hoover chains: The canonical ensemble via continuous dynamics. *J. Chem. Phys.* **97**, 2635–2643 (1992).
58. Togo, A. & Tanaka, I. First principles phonon calculations in materials science. *Scr. Mater.* **108**, 1–5 (2015).
59. Henkelman, G., Uberuaga, B. P. & Jonsson, H. A climbing image nudged elastic band method for finding saddle points and minimum energy paths. *J. Chem. Phys.* **113**, 9901–9904 (2000).
60. Chen, H., Wong, L. L. & Adams, S. SoftBV - a software tool for screening the materials genome of inorganic fast ion conductors. *Acta Crystallogr B Struct. Sci. Cryst. Eng. Mater.* **75**, 18–33 (2019).
61. Momma, K. & Izumi, F. VESTA: a three-dimensional visualization system for electronic and structural analysis. *J. Appl. Crystallogr.* **41**, 653–658 (2008).

Acknowledgements

The professor J.L. is grateful to the financial support from National Key R&D Program of China (2022YFB3807700), National Natural Science Foundation of China, NSFC (22133005, 22403102), Science and Technology Commission of Shanghai Municipality (23ZR1472600, LJ2024049). Y.W. is supported by the Youth Innovation Promotion Association CAS (2022251) and the Shanghai Explorer Program (Batch I)

(23TS1401500). X.Z. is the recipient of Shanghai Sailing Program (24YF2753300), NSFC (22403102) and the Shanghai Super Post-Doctor Incentive Program (2022665).

Author contributions

J.L. designed and supervised this work. R.M. coordinated the experiments, secured funding and contributed to data interpretation. X.Z. performed the experiments and calculations, analyzed the data and drafted the manuscript. Y.L. carried out the EIS experiment. Y.W. and E.S. appraised and revised the paper. All authors discussed the results and reviewed the manuscript.

Competing interests

The authors declare no competing interests.

Additional information

Supplementary information The online version contains supplementary material available at https://doi.org/10.1038/s41467-025-60823-0.

Correspondence and requests for materials should be addressed to Ruguang Ma or Jianjun Liu.

Peer review information *Nature Communications* thanks Gianmarco Taveri, and the other, anonymous, reviewers for their contribution to the peer review of this work. A peer review file is available.